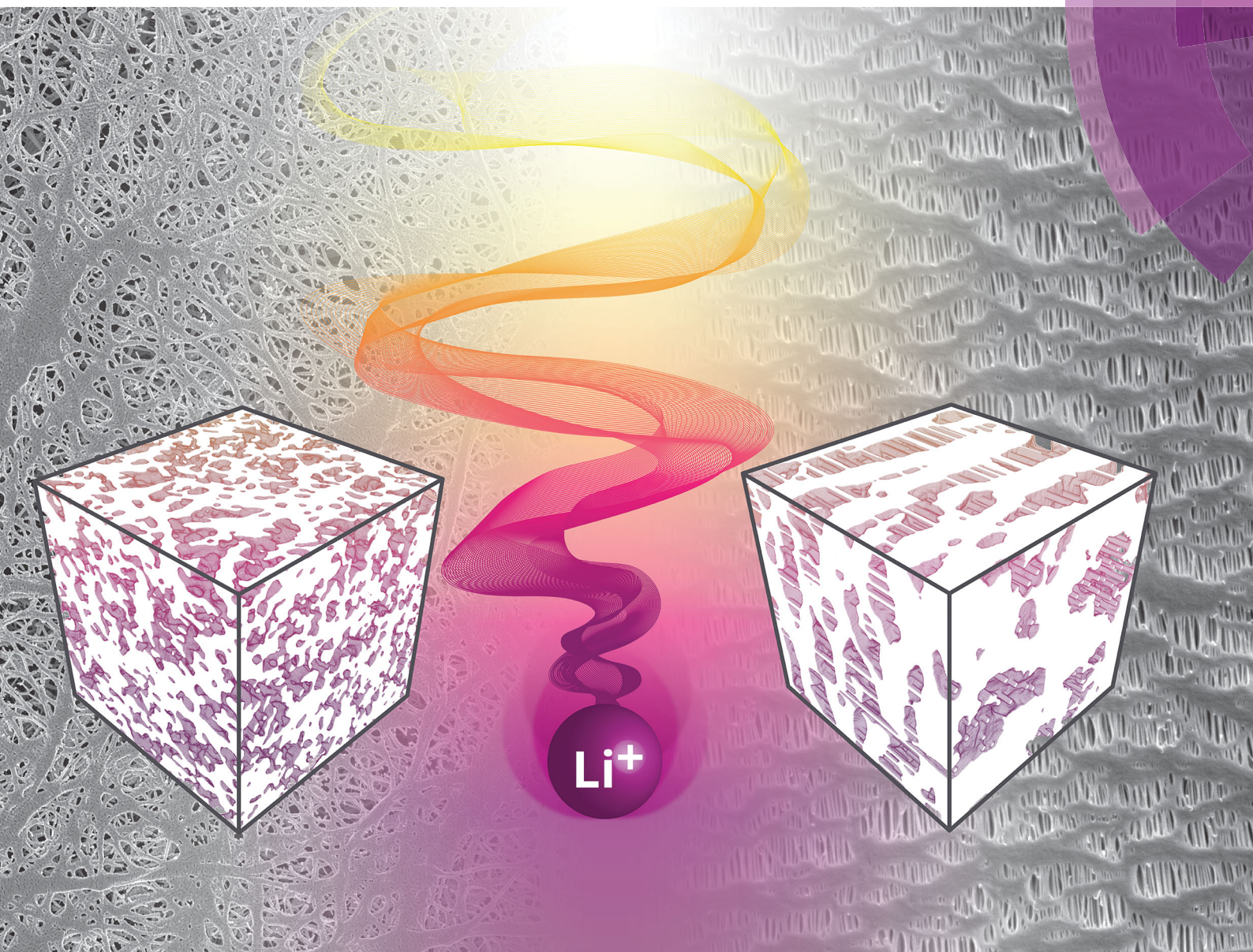


# Energy & Environmental Science

rsc.li/ees



ISSN 1754-5706



**PAPER**

V. Wood *et al.*

Topological and network analysis of lithium ion battery components: the importance of pore space connectivity for cell operation



Cite this: *Energy Environ. Sci.*, 2018, 11, 3194

## Topological and network analysis of lithium ion battery components: the importance of pore space connectivity for cell operation†

M. F. Lagadec,  R. Zahn,  S. Müller and V. Wood \*

The structure of lithium ion battery components, such as electrodes and separators, are commonly characterised in terms of their porosity and tortuosity. The ratio of these values gives the effective transport coefficient of lithium ions in the electrolyte-filled pore spaces, which can be used to determine the ionic resistivity and corresponding voltage losses. Here, we show that these microstructural characteristics are not sufficient. Analysis of tomographic data of commercial separators reveals that different polyolefin separators have similar porosity and through-plane tortuosity, which, in the homogenised picture of lithium ion cell operation, would imply that these different separators exhibit similar performance. However, numerical diffusion simulations indicate that this is not the case. We demonstrate that the extent to which lithium ion concentration gradients are induced or smoothed by the separator structure is linked to pore space connectivity, a parameter that can be determined by topological or network based analysis of separators. These findings enable us to propose how to design separator microstructures that are safer and accommodate fast charge and discharge.

Received 25th March 2018,  
Accepted 28th June 2018

DOI: 10.1039/c8ee00875b

rsc.li/ees

### Broader context

With the rapid growth of the lithium ion battery market and the expansion of the technology to new applications such as electric mobility and grid storage, there is need for better methods to understand and predict cell performance and degradation. In recent years, quantitative imaging techniques have been developed, making it possible to visualise the 3D structure of lithium ion battery materials and components with sub-micron resolution. 3D reconstructions of battery electrodes and separators can be used to quantify their porosity and tortuosity, which are the input parameters for battery simulation tools. Here, we show that porosity and tortuosity are insufficient to predict cell performance and propose the connectivity of the pore space as an additional metric. Our analysis showing how connectivity can be linked to ion concentration distributions in pores is relevant not only for batteries, but for a large number of devices involving ion motion through pores including for example fuel cells, capacitors, water splitting cells, and desalination membranes.

The structures of components in a lithium ion battery (LIB), such as the electrodes and the separator, influence lithium ion transport<sup>1</sup> and therefore play an important role in dictating the cell performance metrics such as (dis)charge-rate dependent capacity and cycle life.<sup>2</sup>

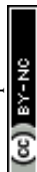
In the homogenised picture of cell operation used in 1D models<sup>3–5</sup> that dominate cell modelling today (e.g., Dualfoil<sup>6</sup> and COMSOL Multiphysics<sup>7</sup>), the diffusion coefficient of the cations ( $D_+$ ) and the anions ( $D_-$ ) in the electrolyte-filled pore

space is given by their diffusion in a bath of electrolyte scaled by the effective transport coefficient of the microstructure,<sup>8</sup>  $\delta_{\text{TP}} = \varepsilon/\tau_{\text{TP}}$ , where  $\varepsilon$  is the porosity and  $\tau_{\text{TP}}$  is the tortuosity along the through-plane (TP) direction between the current collectors. A low effective transport coefficient leads to a low ionic diffusivity and therefore a low ionic conductivity ( $\sigma \approx c \cdot (D_+ + D_-)$ , where  $c$  is the concentration of the salt in the electrolyte), which in turn results in large voltage drops (i.e., large overpotentials) across the electrolyte-filled pore space.<sup>9</sup> At fast operation speeds (e.g., at the end of a 5C discharge),<sup>10</sup> these overpotentials can account for ~60% of cell overpotentials, outweighing the contributions of the charge transference resistance at the electrodes.

However, this volume-averaged effective transport in the homogenised picture does not account for inhomogeneities across the cells. Inhomogeneities lead to incomplete capacity extraction, lithium plating, and hot spots where current

Department of Information Technology and Electrical Engineering, ETH Zurich, Zurich CH-8092, Switzerland. E-mail: vwood@ethz.ch

† Electronic supplementary information (ESI) available: Description of effective transport calculations; Minkowski functionals; algorithm to generate reference structures; shape, network, pore orientation and end-point analysis; steady-state diffusion simulations; algorithm to add nanofibers to PP separator geometry; and evaluation of PP separator without and with nanofibers. See DOI: 10.1039/c8ee00875b





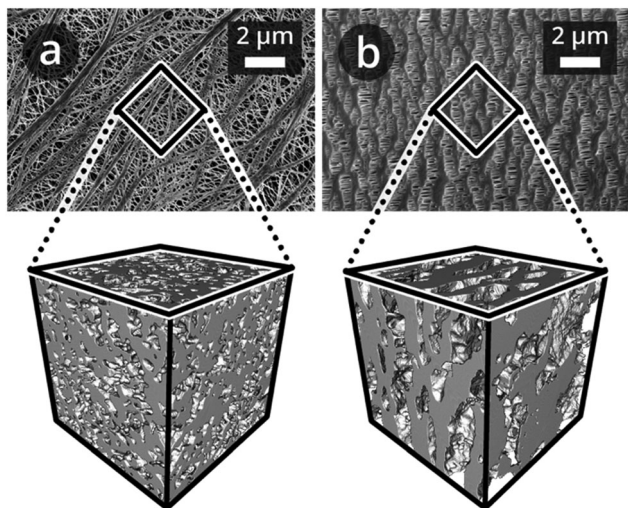


Fig. 1 SEM top view image recorded in secondary electron mode, and 3D microstructure renderings of (a) Targray PE16A and (b) Celgard<sup>®</sup> PP1615 separators of sub-volumes of 3  $\mu\text{m}$  edge length, imaged as described by Lagadec *et al.*<sup>15</sup>

preferentially flows.<sup>11–14</sup> While inhomogeneities can be determined by running simulations over real 3D microstructures<sup>8,11</sup> or statistically assessing many sub-volumes of an imaged microstructure,<sup>15</sup> these analyses do not tell us about how the structure itself may give rise to or how good it is at compensating for inhomogeneities.

In this article, we propose a new approach to characterise microstructure of lithium ion battery components based on topological and network analysis. We show that this analysis captures how a structure induces or homogenises ion gradients.

While topological analysis of porous media is commonly used in soil physics and geology,<sup>16,17</sup> it has not previously been applied to the LIB field. Linked to topology is network theory, which describes the types of connections that exist in a system that can be characterised by branches and nodes (*i.e.*, points where branches intersect). Network analysis has been applied in a wide variety of fields including information and communication (*e.g.*, the world-wide web), energy (*e.g.*, power grids), and biology (*e.g.*, metabolic networks),<sup>18</sup> but not to describe the pore space of a battery, which can also be viewed as a network.

Here, we show that parameters that can be calculated from topological and network analysis of 3D microstructures, such as pore space connectivity density and percent of dead end pores, are important for predicting cell performance and safety.

As a case study, we look at lithium ion battery separators. We show that two separators of strikingly different morphology have similar TP effective transport coefficients, suggesting that both separators would exhibit similar lithium ion transport. However, 3D diffusion simulations highlight that lithium ion transport occurs in different ways in the separator structures. We show that the differences in pore space topology and network properties of the two separators can explain the different transport properties in the separators, particularly the tendency of a

Table 1 Porosity,  $\varepsilon$ , tortuosity,  $\tau$ , and effective transport coefficient,  $\delta$ , for representative volume elements of Targray PE16A<sup>22</sup> (PE) of 2  $\mu\text{m}$  edge length and of Celgard<sup>®</sup> PP1615<sup>23</sup> (PP) of 3  $\mu\text{m}$  edge length. The tortuosity values are obtained from Fickian diffusion simulations across the pore phase in both in-plane directions (IP1 and IP2) and in the TP direction

Parameter	PE	PP
Porosity $\varepsilon$ [%]	40.82 $\pm$ 1.92	40.19 $\pm$ 1.03
Tortuosity $\tau$ [—]	$\tau_{\text{IP1}}$	2.99 $\pm$ 0.39
	$\tau_{\text{IP2}}$	2.65 $\pm$ 0.31
	$\tau_{\text{TP}}$	2.64 $\pm$ 0.21
Effective transport coefficient $\delta$ [%]	$\delta_{\text{IP1}}$	13.9 $\pm$ 2.2
	$\delta_{\text{IP2}}$	15.7 $\pm$ 2.2
	$\delta_{\text{TP}}$	15.6 $\pm$ 1.9

structure to allow or prevent lithium ion concentration gradients. These parameters can be used to optimise separator selection for a given cell and to guide design of next generation separators.

Microporous polyolefin membranes have been used as separators in LIBs for several decades, and have been manufactured with a variety of thicknesses, pore structures, and surface chemistries.<sup>19,20</sup> Recently, we have shown that it is possible to obtain quantitative reconstructions of LIB separators using focus-ion-beam scanning electron microscope (FIB-SEM) tomography.<sup>15,21</sup> 3D microstructure renderings of polyethylene (PE)<sup>22</sup> and polypropylene (PP)<sup>23</sup> separators obtained using this approach are shown in Fig. 1.

The PE and PP separators exhibit distinct morphologies that stem from the different processes used to manufacture them. The PE separator (Fig. 1a) microstructure is isotropic,<sup>15</sup> while that of PP is anisotropic<sup>21</sup> (Fig. 1b). However, the respective porosities,  $\varepsilon$ , TP tortuosities,  $\tau_{\text{TP}}$ , and thus the effective transport coefficients,<sup>8</sup>  $\delta_{\text{TP}} = \varepsilon/\tau_{\text{TP}}$ , of the PE and PP microstructures are similar (Table 1); they are representative of the overall imaged microstructures and in agreement with the manufacturers' specifications.

Topological and network analysis of these structures provides a set of parameters with which to quantify separators. Here, we provide a brief introduction of these parameters for readers unfamiliar with morphological or network descriptors and illustrate simple cases in Fig. 2.

The topological invariant (Euler–Poincaré characteristic, see Sections 2 and 3 in the ESI<sup>†</sup>),<sup>24</sup>  $X$ , describes an object's shape and structure independent of how it is bent and relates to the object's connectivity,<sup>16,25</sup> which is a concept from topology and network theory. The skeleton of the structure (*i.e.*, pink lines in Fig. 2) can be used to analyse the separator as a network.

$X$  of a given pore network is  $N - C$  (see ESI<sup>†</sup>), where  $N$  is the number of unique pores, and  $C$  is their connectivity, which is defined as the number of cuts needed to obtain a simply connected network (*i.e.*, without redundant connections).<sup>26</sup> From network analysis,  $C$  is also defined as the number of branches minus the end point branches (*i.e.*, dead-end branches connected only to a single node) minus number of nodes plus 1.

To illustrate this connection between the topological invariant,  $X$ , and the connectivity,  $C$ , we consider two cases. In Fig. 2a,



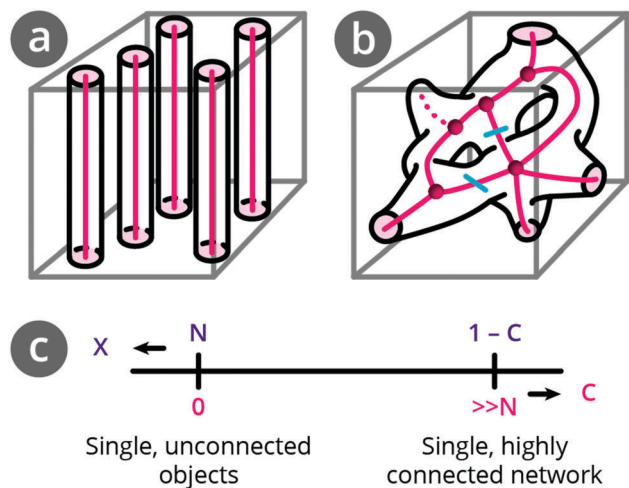


Fig. 2 Schematics of pore space and pore space skeletonisation of (a) unconnected single objects with connectivity  $C = 0$ , and of (b) single, interconnected network (redrawn from DeHoff *et al.*<sup>27</sup> with branches and nodes) connectivity  $C = 2$ . (c) Relationship between Euler–Poincaré characteristic,  $X$ , and connectivity,  $C$ .

we have  $N$  unconnected pores.  $C$  is zero and  $X$  is positive ( $X = N$ ). In the case of a single pore network in Fig. 2b,  $N = 1$  and  $C = 2$  (the two redundant connections are marked with cyan cuts) such that  $X$  is negative ( $X = 1 - 2 = -1$ ). Alternatively, we see that there are 11 branches, 5 end points, and 5 nodes, also giving  $C = 2$ . A more connected network (higher  $C$ ) implies a more negative  $X$  (Fig. 2c).

From network analysis, we additionally consider the node density, the number of nodes of different order (the order is given by the number of branches connected to the node), the number of end point branches, and the average branch length.

In the example in Fig. 2b, we have one node of order 5 and four nodes of order 3. There are 5 end point branches, but, for our purposes, because we only work with a sub-volume of a separator, we count only those that end within the structure as end-point branches (dashed line).

Since the real separator structures are complex, we work with computer-generated, idealised structures as well as with the imaged PE and PP structures.

We generate structures (Fig. 3) with cylindrical pores in 1, 2, and 3 directions using the algorithm described in Section 4 of

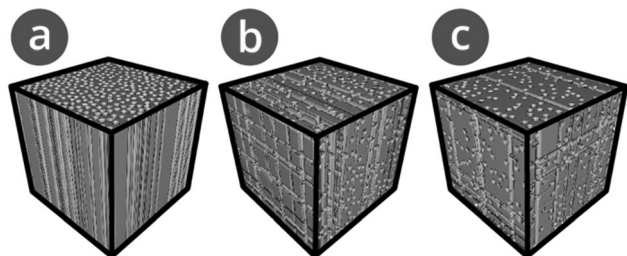


Fig. 3 Example 3D microstructure renderings of artificial separator microstructures with randomly distributed, cylindrical pores of diameter  $0.13 \mu\text{m}$  and edge length  $3 \mu\text{m}$  in (a) one, (b) two, and (c) three dimensions.

the ESI.<sup>†</sup> For each type of structure, 3 entities are generated and the reported properties are the average values. The pore (*i.e.*, cylinder) diameter is comparable to the geometrical pore size,  $D_{50}$ , of the PE separator, and their porosity,  $\epsilon$ , is set to be within  $40 \pm 2\%$ , which is comparable to the porosity of the PE and PP separators. These cubic datasets have an edge length of  $5 \mu\text{m}$  and an isotropic voxel length of  $10 \text{ nm}$ .

For the three computer generated reference structures as well as the imaged PE and PP, we calculate  $X$  using the MATLAB code by Legland *et al.*<sup>25</sup> For the skeleton analysis, the datasets are symmetrically eroded using the 3D thinning algorithm of the Skeletonize 3D plugin in ImageJ. The resulting 3D skeletons are evaluated using ImageJ's AnalyzeSkeleton (2D/3D) plugin to assess the number of branches, nodes, and end-points, and the order of nodes as described in Sections 5 and 6 of the ESI.<sup>†</sup> To determine the proportions of node orders, the inter-trabecular angle calculation program by Reznikov *et al.*<sup>28</sup> is used. We normalise  $X$  and  $C$  by dividing them by the analysed microstructure volume,  $V$ , which gives the corresponding densities  $\chi$  and  $c$  (Table 2).

For unconnected, cylindrical pores in one dimension, we obtain zero connectivity density  $c$  and a positive value for  $\chi$  ( $7.23 \mu\text{m}^{-3}$ ), which corresponds to  $n$ , the number of pores per unit volume  $V$ , since  $\chi = n - c$ . For a single, connected pore network,  $n$  is given by  $N/V$  ( $N = 1$  and  $V = 125 \mu\text{m}^3$  yielding  $n = 0.008 \mu\text{m}^{-3}$ ); therefore,  $\chi$  and  $c$  are almost identical in magnitude but of opposite sign. For interconnected pores in two directions with  $N = 1$ ,  $\chi$  is negative ( $\chi = -102.71 \mu\text{m}^{-3}$ ,  $X = -12838.33$ ) and the connectivity density,  $c$ , is positive ( $c = 102.71 \mu\text{m}^{-3}$ ,  $C = 12839.33$ ), indicating that the number density of redundant connections in the pore network has increased.

The PE microstructure is more connected ( $c = 143.16 \mu\text{m}^{-3}$ ,  $C = 17894.67$ ) than the reference microstructure with pores in 3 directions ( $c = 117.37 \mu\text{m}^{-3}$ ,  $C = 14671.00$ ), which has comparable geometrical pore radius  $D_{50}$ . In contrast, the PP separator exhibits a relatively small negative  $\chi$  ( $\chi = -7.43 \mu\text{m}^{-3}$ ,  $X = -929.00$ ) and a low connectivity ( $c = 7.44 \mu\text{m}^{-3}$ ,  $C = 930.00$ ), which can be understood by noting its straight pores with few redundant connections.

To further understand these trends in connectivity, we systematically analyse the proportions of node order, node and branch densities, percentage of end point branches, and average branch length (Table 3). The reference separator pore networks with pores in two and three dimensions have a similar fraction of nodes of order 3–6 (Section 6 in the ESI<sup>†</sup>) and, as designed, zero end point branches within the volume. As larger numbers of perpendicular pore channels are introduced, the node and branch densities increase and the average branch length decreases. For the reference datasets, the pore dead-ends all are at the dataset's boundaries, whereas for the measured datasets, the pore dead-ends also appear within the volume.

Consistent with its low connectivity, PP exhibits a lower node density and a larger average branch length than the PE separator. Analysis of the pore orientations (Section 7 in the ESI<sup>†</sup>) indicates that PP contains straight pores, while pores in the PE separator are also angled relative to one another.



**Table 2** Average values and standard deviations of porosity, topological invariant density,  $\chi$ , and connectivity density,  $c$ , for the artificially generated microstructures (1D, 2D and 3D) and the imaged Targray PE16A (PE) and Celgard<sup>®</sup> PP1615 (PP) separator microstructures of edge lengths 5  $\mu\text{m}$  each. The values for  $\chi$  and  $c$  are calculated via the Minkowski functional,  $M_3$

Parameter	1D	2D	3D	PE	PP
Porosity [%]	39.95 $\pm$ 0.00	40.48 $\pm$ 0.07	41.04 $\pm$ 0.04	40.53 $\pm$ 0.77	40.19 $\pm$ 0.42
Topological invariant density $\chi$ [ $\mu\text{m}^{-3}$ ]	7.23 $\pm$ 0.00	-102.71 $\pm$ 0.16	-117.36 $\pm$ 1.15	-143.15 $\pm$ 6.88	-7.43 $\pm$ 0.51
Connectivity density $c$ [ $\mu\text{m}^{-3}$ ]	0.00 $\pm$ 0.00	102.71 $\pm$ 0.16	117.37 $\pm$ 1.15	143.16 $\pm$ 6.88	7.44 $\pm$ 0.51

**Table 3** Pore network properties for the artificially generated microstructures with pores in 2 and 3 directions, as well as for Targray PE16A (PE), and Celgard<sup>®</sup> PP1615 (PP). The values are averaged for three datasets of edge length 5  $\mu\text{m}$

Parameter		2D	3D	PE	PP
Proportion [%] of nodes of order	3	74.44 $\pm$ 1.07	74.37 $\pm$ 0.50	80.97 $\pm$ 0.35	89.60 $\pm$ 0.17
	4	24.00 $\pm$ 0.26	22.07 $\pm$ 0.53	15.16 $\pm$ 0.14	9.28 $\pm$ 0.16
	5	0.68 $\pm$ 0.10	2.82 $\pm$ 0.07	3.08 $\pm$ 0.13	1.00 $\pm$ 0.03
	6	0.01 $\pm$ 0.01	0.57 $\pm$ 0.03	0.60 $\pm$ 0.05	0.10 $\pm$ 0.04
Node density [ $\mu\text{m}^{-3}$ ]		171.56 $\pm$ 1.40	187.24 $\pm$ 1.66	282.68 $\pm$ 8.64	36.50 $\pm$ 1.23
Branch density [ $\mu\text{m}^{-3}$ ]		284.35 $\pm$ 2.12	314.46 $\pm$ 2.18	490.03 $\pm$ 14.62	69.87 $\pm$ 2.06
End point branches [%]		0	0	9.07 $\pm$ 0.39	31.55 $\pm$ 0.81
Average branch length [nm]		158.74 $\pm$ 1.35	148.12 $\pm$ 0.62	129.85 $\pm$ 0.42	189.88 $\pm$ 0.92

This difference in how pores are connected in PE and PP separators is further revealed by the different fractions of node orders. PE and PP exhibit ratios of 81 : 15 and 90 : 9, respectively for nodes of orders 3 and 4. The larger number of higher order nodes combined with the larger connectivity in the PE separator compared to the PP separator reflects the high redundancy of connections between nodes and larger spreading power. Thus, on a device level, transport through the separator pore network remains unchanged even if some pores are blocked. Finally, the PP separator exhibits a larger percentage of end point branches within the volume (31.55%) than the PE separator (9.07%), see Section 8 in the ESI.†

To understand the impact of these structural differences on battery performance, we perform steady-state Fickian diffusion simulations on the artificial and measured separator structures. We use cubic datasets of 3  $\mu\text{m}$  edge length and iteratively calculate the solution of the Poisson equation on the electrolyte domain of the input geometry along the TP direction. We use Dirichlet boundary conditions at the end planes orthogonal to the TP direction and zero flux Neumann boundary conditions on all other boundaries and on the separator surfaces.<sup>29,30</sup> Inlet and outlet concentrations of 1.25 and 1.20 M are chosen based on the COMSOL simulation of C-rate dependence of electrolyte

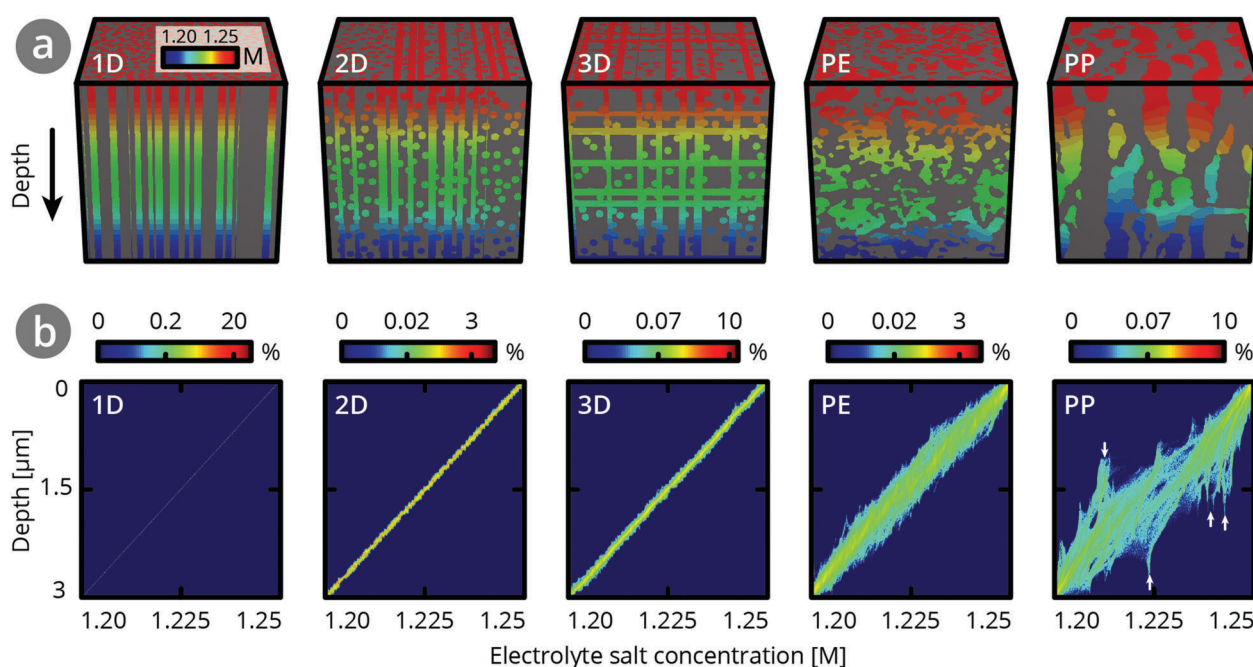


**Fig. 4** (a) Concentration profiles and (b) concentration density maps from steady-state Fickian diffusion simulations across the through-plane direction of artificially generated and recorded datasets of 3  $\mu\text{m}$  edge length with a concentration difference of  $\sim$ 50 mM between top (1.25 M) and bottom (1.20 M).





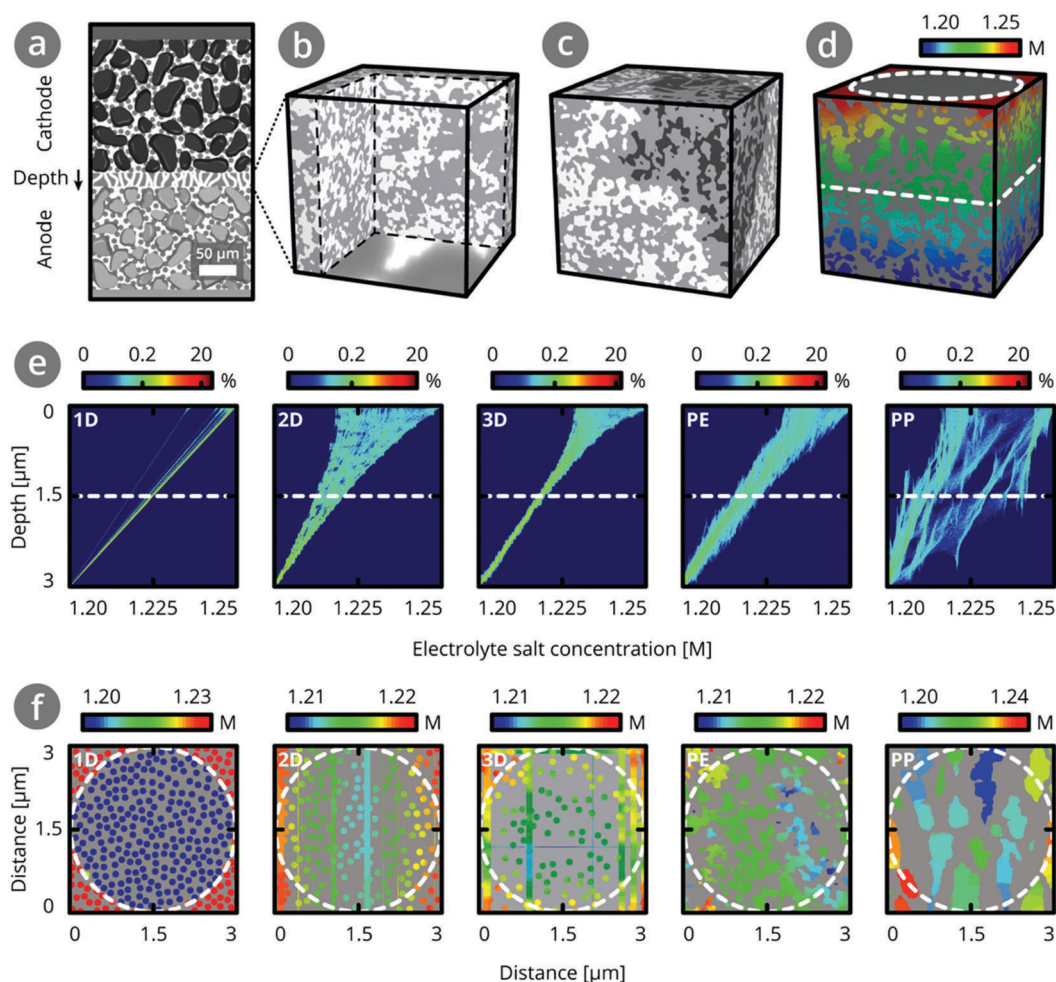
salt concentration for Li<sup>0</sup>|separator|LTO cells with Targray PE16A separator shown in the ESI.†

Fig. 4 shows the concentration profiles and density maps of these simulated, steady-state concentration gradients at different depths in the separator structure, which reveal the influence of separator topology on the concentration distributions. For 1D pores in the TP direction, all cylindrical pore channels have the same concentration at a given depth, so the concentration profile is a straight line. Upon adding more pores in a second and third direction, the concentration profile at a given depth broadens slightly ( $\sim 2$  mM and  $\sim 3$  mM, respectively). For the PE separator, the concentration profile broadens to  $\sim 13$  mM, indicating a variety of ion concentrations in different pores at a given depth. The concentration profile for the PP separator shows a broad distribution of concentrations at each depth. As marked by arrows, there are also regions where the

same electrolyte concentration is found over close to  $1 \mu\text{m}$  in length. This comes from dead-end pores, which extend in the TP direction but lack a connection with other pore channels.<sup>31</sup> Compared to the PE dataset, the PP dataset shows many more such threads, consistent with the network analysis (Table 3).

Assuming PE separator thicknesses of 12–16  $\mu\text{m}$ , we estimate a broadening of 45–60 mM. This corresponds to a range of 23–24% of the calculated concentration differences ( $\sim 190$ –250 mM) at each depth, as outlined in Section 9 in the ESI.† In contrast, for the PP separator, a broadening corresponding to  $\sim 50\%$  of the concentration differences is found. This is consistent with the higher connectivity in the PE separator than the PP separator.

Regions of different electrolyte concentrations may lead to uneven lithium insertion into the electrode material, resulting in uneven expansion, and diffusion induced stress and cracking,<sup>13,32,33</sup> as well as local overcharging or deep discharging. This can



**Fig. 5** (a) Schematic of LIB setup with electrode particles touching the separator. (b) Rendering of separator volume of  $3 \mu\text{m}$  edge length with separator-electrode interface. The electrode particles are of diameters  $3$ – $6 \mu\text{m}$  (*i.e.*, up to three orders of magnitude larger than separator pores)<sup>35</sup> and can thus block a significant number of separator pores. (c) Rendering of separator volume of  $3 \mu\text{m}$  edge length with blocked pores. (d) Concentration distribution from diffusion simulation across separator volume of  $3 \mu\text{m}$  edge length with a defect of diameter  $3 \mu\text{m}$  on top (dashed circle) and at half depth (dashed line at  $1.5 \mu\text{m}$ ). (e) Concentration density maps for steady-state Fickian diffusion simulations across the through-plane directions of the reference datasets with pores in 1D, 2D, and 3D, and the imaged datasets of PE and PP ( $3 \mu\text{m}$  edge lengths). A circular defect structure of  $3 \mu\text{m}$  diameter was placed on top of the structures and a concentration difference of  $\sim 50$  mM was applied between top and bottom. (f) Ion concentration profiles at  $1.5 \mu\text{m}$  depth (dashed white lines in Fig. 5d and e) across sub-volumes of  $3 \mu\text{m}$  edge length. The dashed circle represents the defect structure at  $0 \mu\text{m}$  depth (see Fig. 5d).



diminish battery performance and shorten battery life-time. Therefore, we expect that a highly-connected structure reduces degradation in a battery (Table 2). This highlights the importance of knowing connectivity in a separator structure: the broadening of the local ion concentration distribution across a separator in the TP direction cannot be deduced from the effective transport coefficient  $\delta_{\text{TP}}$ .

In a next step, we assess how efficient the different separator topologies are at smoothing out in-plane ion concentration gradients that impinge on separator structures and are caused, *e.g.*, by blocked pores. In a commercial lithium ion battery (schematic shown in Fig. 5a), active particles in an electrode are typically on the order of 1 to 40  $\mu\text{m}$  in diameter. This means that the electrode pore space structure has typical features approximately one to two orders of magnitude larger than the pore space of the separator. Direct contact between electrodes and separators can result in different concentrations of lithium ions in regions where the separator's pores are blocked by the electrode particles, and concentrations in regions where the electrode's and separator's pores meet. An example of an interface between a graphite electrode and a separator is shown in Fig. 5b. Alternatively, a defect during separator manufacturing or battery assembly (*e.g.*, agglomeration or contamination) as shown in Fig. 5c may result in blocked areas and in decreased performance.<sup>34</sup> Pore-blocking defects can create ion-insulated regions, which locally may lead to high Li-ion concentrations and over-potentials at the distant separator interface. Local defects in separators lead to non-uniform charging and plating around the defect.<sup>12</sup>

To simulate these types of scenarios and gain an understanding of how high connectivity in a structure can help compensate for concentration gradients, we assume that a 3  $\mu\text{m}$  circular object (electrode particle or defect) locally prevents electrolyte from impinging on the separator as shown in Fig. 5d. Fig. 5e shows the concentration density maps as in Fig. 4 and 5f shows the ion concentration profile at 1.5  $\mu\text{m}$  depth for each sub-volume.

For structures with zero connectivity, the blocked pores do not contribute to the effective transport and form an ion-insulated region. For structures with intermediate connectivity in the range of  $>0$  to  $\sim 100 \mu\text{m}^{-3}$  (*i.e.*, the 2D artificial structure or the PP structure, see Sections 10 and 11 in the ESI†), the pore network can compensate for the presence of defect structures at a depth of  $\sim 3 \mu\text{m}$ , while for microstructures with high connectivity in the range of 100 to  $150 \mu\text{m}^{-3}$  (*i.e.*, the 3D artificial structure and PE) are only mildly affected by the presence of defect structures, and the fan-like distortion ends at around 1.5  $\mu\text{m}$ . Due to its many redundant connections and slanted pores, PE is better at equalising in-plane ion gradients than the 3D artificial structures.

## Conclusions

In summary, we quantified the difference in the topological parameters and node structure of PE and PP separators of

comparable porosity, TP tortuosity, and effective transport. High connectivity of the pores, as found in PE separators, enables ion gradients present at the top of the separator to be smoothed out within a fraction of the separator thickness. A structure with multiple straight cylindrical channels, though offering excellent TP tortuosity and effective transport, has zero connectivity density and, due to the likely presence of defects, is more susceptible to Li plating if integrated into a lithium ion battery. In order to understand separator performance and optimise next generation separators for superior performance in cells, connectivity should be considered.

Beyond their function in describing homogenisation of ion concentration gradients through separators as described in detail here, topological and network-based analysis can also be used to predict how a structure will respond to mechanical or thermal stress.<sup>36</sup> By leveraging known trends in how a structure of a given topology shrinks under thermal stress,<sup>37</sup> deforms in response to compressive or tensile stresses,<sup>38,39</sup> or maintains connectivity despite closing of branches or nodes,<sup>36</sup> it will be possible to predict a separator's response to many of the dynamic processes experienced during cell manufacturing and operation.<sup>40</sup>

Connectivity density can be calculated *via* a Minkowski functional and is important when describing homogenisation of ion concentration gradients across microstructures. Similarly, other morphological and topological parameters are helpful when assessing surface interactions and effects.<sup>31,35,41</sup> Among such parameters are other Minkowski functionals, which correspond to a microstructure's surface area and curvature (described in detail in Sections 2 and 3 in the ESI†).

Finally, lithium ion battery separators are just one example of a component in energy and environmental systems that can benefit from the topological and network analysis presented here.<sup>42,43</sup> Connectivity can also improve understanding and design of separators in other electrochemical systems such as fuel cells<sup>44,45</sup> or ion-selective membranes for desalination,<sup>46,47</sup> providing insights such as how thick a membrane should be or how transport paths can be designed to prevent mixing of product/reactant streams. Furthermore, beyond separator technology, we propose that all electrochemical systems (catalysis stacks for fuel generation, sensitised solar cells, lithium ion battery anodes and cathodes, *etc.*) can be viewed as interwoven electronic and ionic networks. An ideal system will have balanced networks at all length scales that bring together (or carry away) electrons and ions (or reactants and products) at equal rates while maintaining mechanical stability.

## Conflicts of interest

There are no conflicts to declare.

## References

- M. A. Martin, C.-F. Chen, P. P. Mukherjee, S. Pannala, J.-F. Dietiker, J. A. Turner and D. Ranjan, *J. Electrochem. Soc.*, 2015, **162**, A991–A1002.



- 2 C.-F. Chen, A. Verma and P. P. Mukherjee, *J. Electrochem. Soc.*, 2017, **164**, E3146–E3158.
- 3 M. Doyle, *J. Electrochem. Soc.*, 1993, **140**, 1526–1533.
- 4 T. F. Fuller, M. Doyle and J. Newman, *J. Electrochem. Soc.*, 1994, **141**, 1–10.
- 5 T. F. Fuller, M. Doyle and J. Newman, *J. Electrochem. Soc.*, 1994, **141**, 982–990.
- 6 Fortran programs for the simulation of electrochemical systems, 2009.
- 7 COMSOL Multiphysics, Batteries & Fuel Cells Module.
- 8 M. Ebner, D. W. Chung, R. E. García and V. Wood, *Adv. Energy Mater.*, 2014, **4**, 1–6.
- 9 J. Newman and W. Tiedemann, *AIChE J.*, 1975, **21**, 25–41.
- 10 R. Chandrasekaran, *J. Power Sources*, 2014, **262**, 501–513.
- 11 S. J. Harris and P. Lu, *J. Phys. Chem. C*, 2013, **117**, 6481–6492.
- 12 J. Cannarella and C. B. Arnold, *J. Electrochem. Soc.*, 2015, **162**, A1365–A1373.
- 13 G. Sun, T. Sui, B. Song, H. Zheng, L. Lu and A. M. Korsunsky, *Extreme Mech. Lett.*, 2016, **9**, 449–458.
- 14 K. Leung and K. L. Jungjohann, *J. Phys. Chem. C*, 2017, **121**, 20188–20196.
- 15 M. F. Lagadec, M. Ebner, R. Zahn and V. Wood, *J. Electrochem. Soc.*, 2016, **163**, A992–A994.
- 16 H.-J. Vogel, U. Weller and S. Schlüter, *Comput. Geosci.*, 2010, **36**, 1236–1245.
- 17 E. Rabot, M. Wiesmeier, S. Schlüter and H.-J. Vogel, *Geoderma*, 2018, **314**, 122–137.
- 18 S. H. Strogatz, *Nature*, 2001, **410**, 268–276.
- 19 P. Arora and Z. Zhang, *Chem. Rev.*, 2004, **104**, 4419–4462.
- 20 S. S. J. Zhang, *J. Power Sources*, 2007, **164**, 351–364.
- 21 D. P. Finegan, S. J. Cooper, B. Tjaden, O. O. Taiwo, J. Gelb, G. Hinds, D. J. L. Brett and P. R. Shearing, *J. Power Sources*, 2016, **333**, 184–192.
- 22 M. F. Lagadec, M. Ebner and V. Wood, *Microstructure of Targray PE16A Lithium-Ion Battery Separator*, ETH Zurich, 2016, DOI: 10.5905/ethz-1007-32.
- 23 M. F. Lagadec and V. Wood, *Microstructure of Celgard<sup>®</sup> PP1615 Lithium-Ion Battery Separator*, ETH Zurich, 2018, DOI: 10.3929/ethz-b-000265085.
- 24 C. Scholz, F. Wirner, J. Götz, U. Rude, G. E. Schröder-Turk, K. Mecke and C. Bechinger, *Phys. Rev. Lett.*, 2012, **109**, 264504.
- 25 D. Legland, K. Kiêu and M. F. Devaux, *Image Anal. Stereol.*, 2007, **26**, 83–92.
- 26 J. C. Russ, *The Image Processing Handbook*, CRC Press, Taylor & Francis Group, 2016.
- 27 R. T. DeHoff, E. H. Aigeltinger and K. R. Craig, *J. Microsc.*, 1972, **95**, 69–91.
- 28 N. Reznikov, H. Chase, Y. Ben Zvi, V. Tartle, M. Singer, V. Brumfeld, R. Shahar and S. Weiner, *Acta Biomater.*, 2016, **44**, 65–72.
- 29 D. Kehrwald, P. R. Shearing, N. P. Brandon, P. K. Sinha and S. J. Harris, *J. Electrochem. Soc.*, 2011, **158**, A1393–A1399.
- 30 M. Ebner, *Designing Better Batteries: Visualization and Quantification of Microstructure and Degradation Mechanisms in Lithium Ion Battery Electrodes*, PhD thesis, ETH Zürich, 2014, DOI: 10.3929/ethz-a-010211757.
- 31 R. Zahn, M. F. Lagadec and V. Wood, *ACS Energy Lett.*, 2017, **2**, 2452–2453.
- 32 K. Zhao, M. Pharr, S. Cai, J. J. Vlassak and Z. Suo, *J. Am. Ceram. Soc.*, 2011, **94**, 226–235.
- 33 L. Ji, Z. Guo and Y. Wu, *Energy Technol.*, 2017, **5**, 1702–1711.
- 34 D. Mohanty, E. Hockaday, J. Li, D. K. Hensley, C. Daniel and D. L. Wood III, *J. Power Sources*, 2016, **312**, 70–79.
- 35 S. Müller, J. Eller, M. Ebner, C. Burns, J. Dahn and V. Wood, *J. Electrochem. Soc.*, 2018, **165**, A339–A344.
- 36 M. F. Lagadec, R. Zahn and V. Wood, *J. Electrochem. Soc.*, 2018, **165**, A1829–A1836.
- 37 C. T. Love, *J. Power Sources*, 2011, **196**, 2905–2912.
- 38 J. Cannarella, X. Liu, C. Z. Leng, P. D. Sinko, G. Y. Gor and C. B. Arnold, *J. Electrochem. Soc.*, 2014, **161**, F3117–F3122.
- 39 X. Zhang, E. Sahraei and K. Wang, *Sci. Rep.*, 2016, **6**, 32578.
- 40 X. Zhang, J. Zhu and E. Sahraei, *RSC Adv.*, 2017, **7**, 56099–56107.
- 41 R. Zahn, M. F. Lagadec, M. Hess and V. Wood, *ACS Appl. Mater. Interfaces*, 2016, **8**, 32637–32642.
- 42 L. T. Choong, P. Yi and G. C. Rutledge, *J. Mater. Sci.*, 2015, **50**, 3014–3030.
- 43 T. Müllner, K. K. Unger and U. Tallarek, *New J. Chem.*, 2016, **40**, 3993–4015.
- 44 H. Ostadi, P. Rama, Y. Liu, R. Chen, X. X. Zhang and K. Jiang, *J. Membr. Sci.*, 2010, **351**, 69–74.
- 45 J. Joos, M. Ender, I. Rotscholl, N. H. Menzler and E. Ivers-Tiffée, *J. Power Sources*, 2014, **246**, 819–830.
- 46 V. M. Calo, O. Iliev, Z. Lakdawala, K. H. L. Leonard and G. Printsypar, *Int. J. Adv. Eng. Sci. Appl. Math.*, 2015, **7**, 2–13.
- 47 X. Zhao, J. Li and C. Liu, *Desalination*, 2017, **408**, 102–109.

